CHARITÉ
UNIVERSITÄTSMEDIZIN BERLIN

International Graduate Program Medical Neurosciences

Lab Report

Electrophysiological characterization of a GluA4 γ-2 receptor complex and investigation of first event amplitudes in single channel recordings

By: Lukas Born
Matriculation Number: 4003940
Date of submission: 30.09.2024

Keywords:

Scientific Topic (3-5 keywords):
transmembrane auxiliary AMPA proteins, AMPA subconductance levels, single channel recordings

Methods (3-5 keywords):
Macroscopic patch clamp recordings, single channel patch clamp recordings, cell culture, computational data analysis

Please tick 2 fields at max.:

☒ Cellular Neuroscience   ☐ Clinical/Translational Neuroscience
☒ Molecular Neuroscience   ☐ Cognitive Neuroscience
☐ Systems Neuroscience   ☐ Computational Neuroscience

Direct supervisor: Dr. Jenn Noonan

Lab Leader:
Prof. Dr. Andrew Plested
Leonor-Michaelis Haus (18),
Philippstr. 13,
10117 Berlin
andrew.plested@hu-berlin.de

Suggested Second Reviewer:
Prof. Jelena Baranovic
M. Swann Building, 3.25
Max Born Crescent
Edinburgh
jelena.baranovic@ed.ac.uk

1 Introduction

1.1 AMPA function, significance and structure

The α-amino-3-hydroxy-5-methyl-4-isoxazolepropionic acid receptors (AMPAR) are a type of ionotropic glutamate receptor (iGluR), which also include N-methyl-D-Aspartate (NMDA), kainite and GluD receptors. During glutamatergic signaling, glutamate (Glu) gets released from the presynapse, diffuses across the synaptic cleft and binds to receptors. iGluRs undergo conformational rearrangement upon glutamate binding, which opens an ion pore, causing cation influx across the negatively polarized postsynaptic membrane, leading to depolarization (Baranovic et al., 2016; Collingridge & Lester, 1989; Dingledine et al., 1999; Meldrum, 2000; Traynelis et al., 2010). AMPARs are the fastest of the iGluRs, activating within 200-600 µs of Glu application, and almost completely desensitize within tens of milliseconds (Colquhoun et al., 1992; Geiger et al., 1995; Silver et al., 1992). This allows AMPARs to closely follow presynaptic input with the temporal accuracy necessary for precise high frequency signal transduction between neurons.

AMPARs are tightly regulated via subunit composition, phosphorylation or via interactions with other proteins (Anggono & Huganir, 2012; Derkach et al., 2007; Huganir & Nicoll, 2013). Changes in localization, number and kinetics of AMPARs cause alterations in properties of synapses themselves, like long-term potentiation (LTP) or long-term depression (LTD), and are thus involved in several fundamental brain processes like acquisition and storage of memories (Huganir & Nicoll, 2013; Italia et al., 2021; Krugers et al., 2010; Pereyra & Medina, 2021; Sanderson et al., 2008). Given their importance and high degree of regulation, their dysfunction is involved in several CNS pathologies, like Alzheimer's Disease, Parkinson's Disease and Schizophrenia, among others (Italia et al., 2021; Lewis & Moghaddam, 2006; Picconi et al., 2012; Zarate & Manji, 2008; Zeppillo et al., 2022).

AMPARs are composed as homo- or heterotetramers of four subunits (A-D), of which four subtypes exist: GluA1-4. The receptor complex consists of two dimers A+B, C+D, which in turn dimerize. Each subunit is composed of three domains: a transmembrane domain (TMD), a ligand-binding domain (LBD), and an amino-terminal domain (ATD) (Sobolevsky et al., 2009). (Figure 1 left) The function of the ATD remains unclear, as its deletion causes no change in receptor function, but it has been proposed to play a role in receptor assembly and trafficking (Greger et al., 2017; Herguedas et al., 2013). The LBD is comprised of two segments, which form a clamshell shape, with a Glu binding site in between the two lobes of the clamshell site (Armstrong & Gouaux, 2000; Stern-Bach et al., 1998). The TMD is composed of four helices and contains the highly conserved nonselective cation pore, as well as the channel gating site (Kuner et al., 2003; Partin et al., 1995; Sobolevsky et al., 2009). Three of these helices (M1,

M3, M4) completely transverse the membrane, while the M2 helix does not (Sobolevsky et al., 2009). (Figure 1 right)
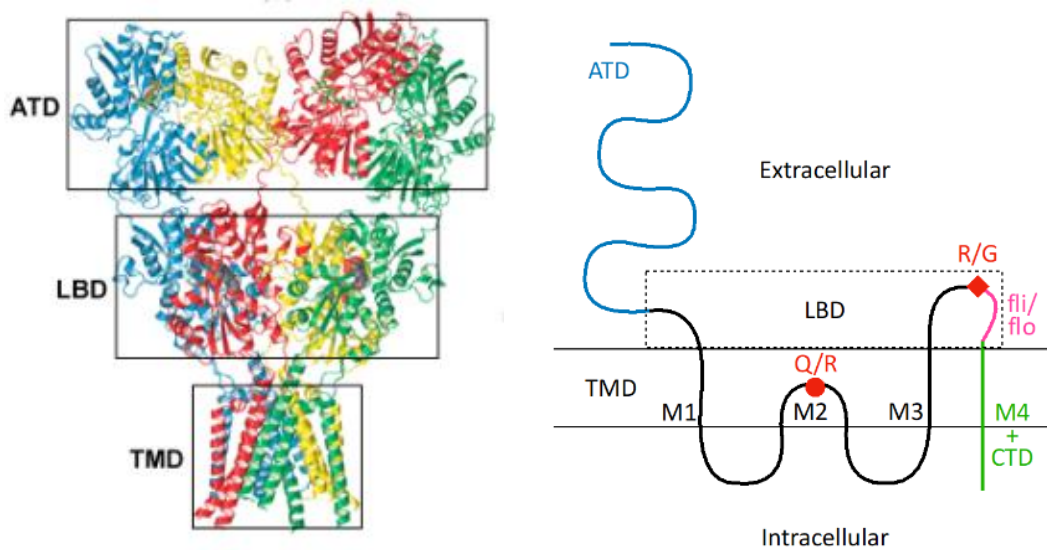
Figure 1. left: Crystal structure of AMPAR. Each color represents a different receptor subunit, Taken from (Sobolevsky et al., 2009) *right: Schematic representation of an AMPAR subunit. Taken from* (Braunbeck, 2022)

Endogenous polyamines, like spermine, can bind to the ion pore in AMPARs, causing a voltage dependent block of ion flow. In GluA2 subunits, this polyamine block can be reversed, by posttranslational RNA modification of an exon that codes for a critical residue, the Q/R site on the M2 helix of the TMD. (Figure 1 right) Editing at the Q/R site causes exchange of the amino acid glutamine (Q) to arginine (R), which causes insensitivity to polyamine block, and also impermeability to divalent cations like Ca^{2+}. Almost all GluA2 subunits are Q/R edited at physiological conditions, the expression of GluA2 subunits, and their integration into synaptic receptors can cause large functional differences between AMPARs (Bowie, 2018).

1.2 Transmembrane AMPAR regulatory proteins

AMPARs are regulated by binding to auxiliary subunits, for example transmembrane AMPAR regulatory proteins (TARPs) like γ-2, also known as stargazin, or γ-8, among many others (Bats et al., 2007, Payne 2008). TARPs not only anchor the receptor at the synapse but can also alter receptor dynamics and kinetics (Priel et al.2005, Coombs et al., 2017). For example, TARPs can attenuate the polyamine block, likely by reducing pore architecture (Bowie 2018). In addition, AMPARs in complex with γ-8 have been shown to produce a desensitization-resistant response after 10-25 Hz applications of glutamate, resulting in a distinct "pedestal" current (Plested and Carbone 2016). In hippocampal synapses, where γ-8 is highly expressed (Rouach et al., 2005; Yamasaki et al., 2016), this pedestal AMPA current was found to be widespread, with a sparse and flat spatial distribution (Pampaloni et al., 2021). Interestingly,

different synapses within the same neuron showed different levels of pedestal response, and activation of synapses that displayed pedestal response could reliably trigger action potentials (Pampaloni et al., 2021). Thus, TARPs could provide a unique, NMDAR-independent postsynaptic mechanism for altering AMPAR responses in individual synapses, and could have unique roles in neural function. However, the exact electrophysiological properties of many TARP-AMPAR complexes remain largely unstudied. The combination of GluA4 receptors and γ-2 was a promising candidate for pedestal currents, as it has previously been shown in single channel recordings that receptor complex promotes high open probability modal gating (Zhang et al., 2014).

In this work, I set out to electrophysiologically characterize the combination of homotetrameric GluA4 AMPARs with the TARP γ-2. To this effect, I used a tandem construct that consisted of GluA4 linked at the C-terminus via a 12 amino acid linker to the N-terminus of γ-2 (A4G2). This ensured equal stoichiometry of both proteins, and complete association γ-2 to every GluA4 subunit, reducing excess TARP toxicity. As control, I used homotetrameric GluA4 AMPAs (A4). In addition, to learn patching and to serve as a further control, I used homotetrameric GluA2 AMPARs (A2). I expressed these receptors in HEK293 cells and recorded their macroscopic responses to glutamate exposure from outside-out patches.
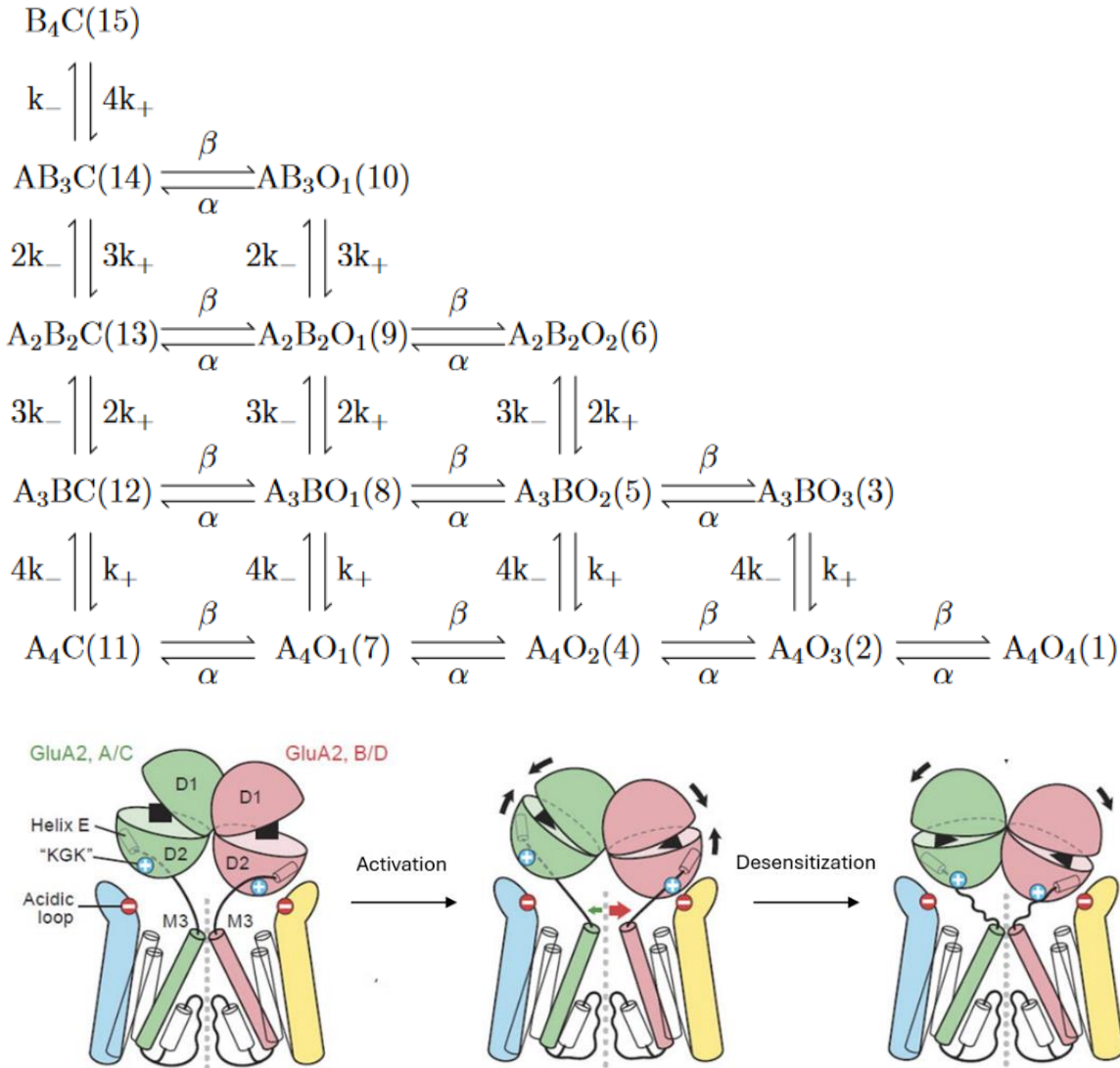
1.3 Exact gating mechanisms of AMPAR

Electrophysiological measurements from single ion channels provide a unique opportunity for studying the exact mechanisms underlying gating and other processes. The amplitude distribution of traces can directly give insight to possible subconductance states. Eleven years before the first full-length crystal structure (Sobolevsky et al., 2009), single channel recordings revealed its tetrameric arrangement. (Rosenmund et al., 1998) demonstrated four distinct subconductance states of desensitization resistant AMPARs during a stepwise activation protocol in single channel recordings. These four subconductance states have been proposed to correspond with four separate open conformations of the receptor, one for each agonist-bound subunit (Blanke & VanDongen, 2009; Rosenmund et al., 1998; Swanson et al., 1997).

In addition, further receptor states can be resolved by examining the different exponential components of time-dwell distributions for open and shut states in idealized traces. By defining hidden Markov models of receptor activation, predicting the time dwell distributions for these models, and fitting them to the observed distributions, one can even calculate rate constants for transitions between proposed states. (Fig. 2 top)

Combining results from structural analysis, single channel recordings and molecular dynamics simulations has allowed for a detailed description of the conformational rearrangements that lead to AMPAR gating and desensitization. Upon binding glutamate, the clamshell of the LBD

closes, and the D1 lobes of the LBD dimerize, pulling open the linkers between the LBD and the TMD, which pulls open the ion channel (Chen et al., 2017). The degree of LBD clamshell closure is agonist dependent, has been shown to directly influence open probability, and correlates with gating (Armstrong & Gouaux, 2000).When the dimer ruptures, the LBDs turn downwards, closing the channel again, which causes desensitization (Armstrong & Gouaux, 2000; Chen et al., 2017; Plested & Mayer, 2009). (Fig. 2 bottom)

$B_4C(15)$

$AB_3C(14) \underset{\alpha}{\overset{\beta}{\rightleftharpoons}} AB_3O_1(10)$

$A_2B_2C(13) \underset{\alpha}{\overset{\beta}{\rightleftharpoons}} A_2B_2O_1(9) \underset{\alpha}{\overset{\beta}{\rightleftharpoons}} A_2B_2O_2(6)$

$A_3BC(12) \underset{\alpha}{\overset{\beta}{\rightleftharpoons}} A_3BO_1(8) \underset{\alpha}{\overset{\beta}{\rightleftharpoons}} A_3BO_2(5) \underset{\alpha}{\overset{\beta}{\rightleftharpoons}} A_3BO_3(3)$

$A_4C(11) \underset{\alpha}{\overset{\beta}{\rightleftharpoons}} A_4O_1(7) \underset{\alpha}{\overset{\beta}{\rightleftharpoons}} A_4O_2(4) \underset{\alpha}{\overset{\beta}{\rightleftharpoons}} A_4O_3(2) \underset{\alpha}{\overset{\beta}{\rightleftharpoons}} A_4O_4(1)$

Figure 2. top: Proposed Markov Model for AMPAR sublevel activation. A_iB_j indicates that i agonist-bound and j unbound subunits comprise the receptor, with α and β being the agonist binding constant. O_1-O_4 indicates the subconductance state and C the closed state. Adapted from (Kuru, 2024) bottom: Activation and desensitization mechanism of AMPAR. Schematic representation of the conformational changes underlying AMPAR activation and desensitization. Depicted are the TMDs and LBDs of one dimer (A/C (green), B/D (red)) and two TARP γ-2 (blue, yellow). Adapted from (Chen et al., 2017)

By applying different molecules or editing some residues in the AMPAR itself, certain states can be stabilized, prolonging the receptors occupancy in this state, which causes downstream

electrophysiological effects. For example, cyclothiazide (CTZ) binds to and stabilizes the activitied dimerized LBD confirmation, which blocks desensitization (Fucile et al., 2006). The T1 mutant, initially characterized in (Baranovic et al., 2016), has three residues mutated to histidine: D668H, T672H, and K761H. When present, these residues chelate zinc, crosslinking the LBD in a tight conformation. By constraining them with zinc, the activation kinetics of AMPAR are slowed down, which makes the T1 mutant an interesting candidate for studying pre-active conformations in AMPARs (Baranovic et al., 2016; Braunbeck, 2022).

In NMDARs, two pre-active conformations have been demonstrated, with rate constants of τ_1 = 7.1 ms and τ_2 = 337.4 ms (Esmenjaud et al., 2019). Because WT AMPARs activate too fast to resolve pre-active states, T1's slower activation kinetics have facilitated the study of these pre-active states. In his 2022 dissertation, Sebastian Braunbeck recorded from single AMPARs, WT and T1, in the presence of 100 µM CTZ to block desensitization and either zinc or EDTA (a zinc chelating agent). He was able to resolve three different pre-active states in the first latency distribution of T1 mutant AMPARs in zinc and CTZ (Braunbeck, 2022).

His recordings provide a rich data set, from which further insights can be gained. In this work, using his data, I set out to find a working definition of the first event, to characterize the distribution of idealized amplitude of the first event, and to find the first latency distributions separately for each of the first event amplitudes.

2 Materials and Methods

2.1 Cell Culture

The human embryonic kidney 293 (HEK293) cell line was used for all patch clamp experiments. All cells were cultured in Modified Eagle Medium (MEM) supplemented with 6% fetal bovine serum (FBS) in T-25 flasks and incubated at 37ºC and 5% CO_2. Cells were split approximately twice a week, when the confluency reached ~90%. The cells were washed with 5 mL of Dulbecco's phosphate buffered saline (DPBS) and incubated on 250 µL 0.05% Trypsin / 0.02% EDTA at 37ºC for 3 minutes. Afterwards the cells were suspended in 10 mL MEM + 6% FBS to stop trypsination, after which they were centrifuged at 100g for 5 minutes. Supernatant was discarded and the cells were resuspended in 5 mL MEM + 6% FBS and split 1:7 - 1:11 (depending on confluency) into a new T-25 flask.

Two days before transfection, 30 – 200 µL of cell suspension (depending on confluency) were seeded onto a ø25 mm dish containing 2 mL MEM + 6% FBS and ~4 ø10 mm coverslips coated with Poly-L-Lysine. These coverslips had been previously sonicated for 15 minutes in 70% ethanol and had been kept in 99% ethanol at room temperature. For coating, coverslips were flamed and put into ø35 mm dishes. Subsequently, ~200 µL of 0.01% Poly-L-Lysine solution were added to the coverslip, incubated at room temperature for 3 minutes, and

removed. After washing twice in 2 mL DPBS, the dishes with coated coverslips were stored at 4°C for up to 4 weeks.

2.2 Transfection

6 µL of polyethylenimine (PEI) solution were added to 192 µL of OPTI-MEM (MEM without phenol red) and incubated for 3 minutes at room temperature. 2 µL of 1 ng/µl plasmid solution, totalling 2 ng DNA, were added and incubated for another 20 minutes at room temperature. The total mixture was then added dropwise to the cells and incubated for 5-12 hours at 37°C. Afterwards, the transfection medium was removed, the cells were washed twice in 2 mL DPBS prior to adding 2 mL of fresh medium supplemented with 30 µL 2 mM NBQX disodium solution in water for a total concentration of 30 µM.

The plasmids that were used for the A2 condition coded for GluA2 (Q) flip and GFP, both under an IRES promoter. The A4 condition plasmids contained GluA4-flip under an IRES promoter and were cotransfected 1:1 with a plasmid coding for GFP under an IRES promoter. The A4G2 condition coded for GluA4-flip linked at its C-terminus via a 12 amino acid linker (Ser-Arg-Gly-Gly-Gly-Gly-Gly-Gly-Thr-Gly-Ala-Thr) to the N-terminus of γ-2 without the start codon and GFP, both under an IRES promoter.

2.3 Electrophysiological setup

Recordings were done 16-48 hours after transfection. Data was collected on the same electrophysiology setup using an Axopatch 200B patch clamp amplifier and amplifier output was monitored on a Tektronix TBS1102B digital oscilloscope. Digitization was performed using a HEKA InstruTECH ITC-18 interface.

Patch pipettes were pulled using a Sutter P-1000 pipette puller from World Precision Instruments TW150F3 3-inch borosilicate glass capillaries, with an outer diameter of 1.5 mm and an inner diameter of 1.12 mm. Electrodes had previously been made from Teflon coated silver wire tipped with a silver chloride pellet. The head stage containing the electrode holder was moved using a Scientifica PatchStar micromanipulator. Pipettes typically had resistances of 3-6 MΩ, and were mounted onto a G23 Instruments electrode holder after being filled with intracellular solution. GluA2 was patched with intracellular solution without spermine (NaCl: 115 mM; NaF: 10 mM; Na_4BAPTA: 5 mM; $CaCl_2$: 0,5 mM; $MgCl_2$: 1 mM; HEPES: 5 mM; Na_2ATP: 10 mM, adjusted to pH 7.2 with NaOH), while both other conditions were patched with intracellular solutions containing spermine (NaCl: 125 mM; NaF: 10 mM; Na_4BAPTA: 5 mM; $CaCl_2$: 0.5 mM; Spermine: 0.1 mM; HEPES: 5 mM; adjusted to pH 7.2 with NaOH).

Solution exchange was achieved using a Physik Instrumente piezoelectric stack actuator, which received 4 V pulses from the acquisition software, transmitted by a Siskiyou controller.

The actuator moved a perfusion tool, which had been made in the lab as laid out in detail in (Braunbeck, 2022), exposing the stationary patch pipette to two different extracellular solutions (NaCl: 150 mM; $MgCl_2$: 0.1 mM; $CaCl_2$ 0.1 mM; HEPES. 5 mM; titrated to pH 7.3 with NaOH). The second solution additionally contained 10 mM glutamate for receptor activation and 2.5 mM sucrose to make the boundary between solutions easier to distinguish under the microscope.

For patching, coverslips containing cells were removed from the incubator and placed into a fresh ø35mm dish containing Solution 1 mounted on a Zeiss Axiovert 100 microscope in a TMC Faraday cage on a TMC vibration-free table. eGFP fluorescence was examined using blue excitation light emitted by an X-Cite series 120Q. Healthy looking, transfected cells were selected by visual inspection. After an outside-out patch had been excised, the solution flow through the perfusion tool was started. After the recordings, the bath solutions were replaced to keep extracellular glutamate solutions low. All data was acquired using the AxoGraph acquisition software (AxoGraph Scientific) at 40kHz after passing through an 8-pole Bessel filter at 10 kHz. The speed of solution exchange and positioning of the patch pipette was tested by applying the solutions to an open tip patch after recording.

2.4 Electrophysiological recordings

For recording, several different protocols were used. To study rise time, peak current, and steady state current, as well as to investigate the kinetics of both desensitization and decay of the receptor response, a 500 ms pulse of glutamate was applied 20 times. To measure the decay of a more physiologically relevant activation, a 2 ms pulse of glutamate was applied 20 times. To measure the recovery from desensitization, a protocol with an initial 500 ms pulse of glutamate was applied, followed by eleven 25 ms pulses, with incrementally more time in between each pulse: 25 ms, 100 ms, 225 ms, 400 ms, 625 ms, 900 ms, 1225 ms, 1600 ms, 2025 ms, 2500 ms and 3025 ms. This incremental protocol was applied 10 times. To measure desensitization in a more physiologically relevant manner than sustained glutamate exposure, 2 ms glutamate pulses were applied at 10 Hz, 20 Hz and 50 Hz for 5 seconds, 5 times respectively. All protocols were recorded at both a holding potential of -60 mV, as well as +50 mV, in so far as this was possible for each patch.

To measure the voltage dependency of the current, the holding potential of the patch was successively set to a series of values: -100 mV, -80 mV, -60 mV, -40 mV, -20 mV, 0 mV, 20 mV, 40 mV, 60 mV, 80 mV and 100 mV for 500 ms, 55 ms after the begin of the holding potential being set which a 400 ms glutamate pulse was applied. Because not enough recordings were available for the A4 condition to be analyzed, despite much effort, recordings that had previously been done in the lab were included in the analysis for this work.

2.5 Data Analysis

Macroscopic current recordings were selected, averaged and baseline corrected in AxoGraph. Subsequently, statistical calculations like 10-90% rise time, peak current, average steady state current, as well as event detection were all performed using IgorPro64 (Wavemetrics, version 9.05) and compiled in Microsoft Excel (Version 2408). Similarly, a double exponential function with y-offset ($f(x) = y_0 + \alpha_1 e^{-\frac{x-x_0}{\tau_1}} + \alpha_2 e^{-\frac{x-x_0}{\tau_2}}$) were fitted to the trace in IgorPro64, α and τ values were exported into Microsoft Excel, where the weighted τ was calculated using the following formula: $\tau_{weighted} = \frac{\alpha_1\tau_1 + \alpha_2\tau_2}{\alpha_1\alpha_2}$. The code for further analysis and data visualization was written in python version 3.10.14 (Van Rossum & Drake, 2009), using the python matplotlib library (Hunter, 2007), and is publicly available on the GitHub repository https://github.com/LukBorn/ASCAM .

2.6 Single channel analysis

All analysis for the single channel project was written in python. For most of the final data analysis, the python program ASCAM (https://github.com/AGPlested/ASCAM) was used. Data and results were visualized using the matplotlib library. The code is publicly available on the GitHub repository https://github.com/LukBorn/ASCAM .

For this project, all data, with a convenient overview spreadsheet, was available on the lab server, and had been previously recorded and analyzed as laid out in (Braunbeck, 2022). In brief, traces were selected, gauss filtered at 1000-2000 kHz and baseline corrected in ASCAM before further analysis. Activation time was determined in ASCAM via automated threshold crossing algorithm, with a different threshold determined for each recording (~-0.5 pA). Idealization was also performed via automated threshold crossing algorithm, with one closed and four open states, with conductances in the range 0, -0.6, -1.2, -1.8, -2.5 (Rosenmund et al., 1998), determined individually for each recording, with a resolution of 130 μs, meaning that events shorter than 130 μs were not counted as events.

In total, five total usable recordings existed of the T1 in EDTA+CTZ condition. Analysis of activation time had been done for all five recordings, summarized in a .csv file containing activation time for each episode. Idealization had been conducted on three of five recordings, and a list of all events containing amplitude, start and end time, duration and episode number. Similarly, for the T1 in zinc+CTZ condition, nine usable recordings existed, of which seven had been analyzed for activation time and three had been idealized. For first event analysis, only those recordings for which both activation time and events .csv files existed were utilized, totaling three per condition. Of both the WT in EDTA+CTZ condition, and the WT in zinc+CTZ condition, several recordings existed, none of which had been idealized however, so they were not included in further analysis.

3 Results

3.1 Sample recordings
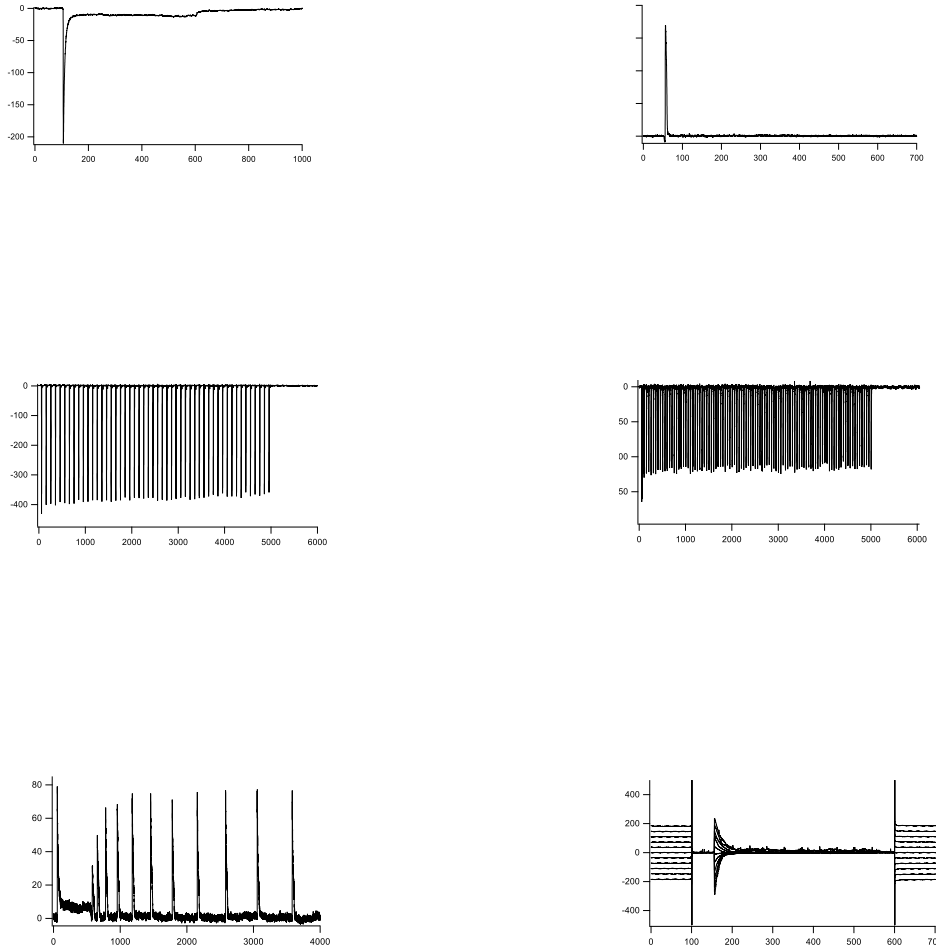
Figure 3. Sample recordings. top left: 500 ms glutamate exposure. *A4G2 condition at -60 mv holding potential, averaged over 20 episodes. Recording 11 from 1.8.2024.* ***top right.: 2 ms glutamate exposure.*** *A4 condition at 50 mV holding potential, averaged over 20 episodes. Recording 24 from 23.8.2024.* ***middle left: 10 Hz pulse train.*** *A2 condition at -60 mV holding potential, averaged over 5 episodes. Recording 7 from 26.7.24.* ***middle right: 20 Hz pulse train.*** *A4G2 condition at -60 mV holding potential, averaged over 5 episodes. Recording 25 from 25.7.24.* ***bottom left: Incremental protocol.*** *A4G2 condition at 50 mV holding potential, averaged over 10 episodes. Recording 46 from 1.8.24.* ***bottom right: Voltage dependency protocol.*** *A2 condition. Recording 13 from 26.7.24.*

## 3.2 GluA4 γ-2 tandem kinetics

No significant differences existed between the rise times of all conditions (Fig 4. left), determined by Kruskal-Wallis test (p-value = 0.26128). All rise times fell in the range of 0 – 2.5 ms which was close to the literature value of 200 - 650 µs (Colquhoun et al., 1992), except for one outlier in the A4 -60mV condition. For peak current (Fig 4. middle), no significant differences could be found between any of the conditions, determined by Kruskal-Wallis test (p-value = 0.07955). As the peak current is mostly a direct result of patch quality, this result can be taken as a confirmation of the comparability of the data gathered. The steady state current (Fig 4. right) also showed no significant difference between all conditions, determined by Kruskal-Wallis test (p-value = 0.26088).
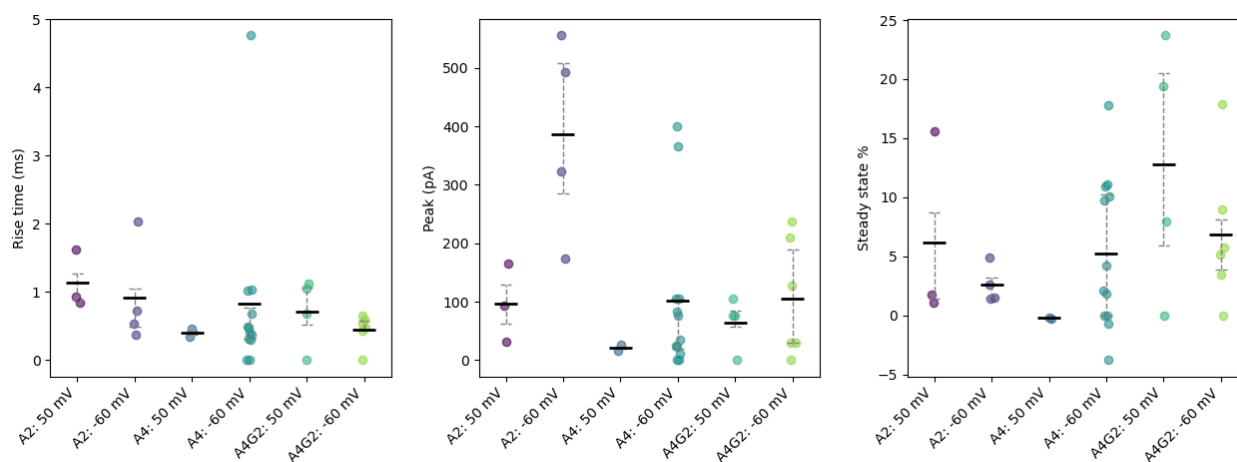
Figure 4. left: Rise time. Time (ms) from 10% to 90% of peak current for the activation upon glutamate exposure. *middle: Peak current.* Peak amplitude (pA) of the activation upon glutamate exposure. *right: Steady state current.* Mean current upon reaching equilibrium after receptor desensitization, normalized to peak current, in %. A2 50mV: n=3. A2 -60mV: n=4. A4 50mV: n=2. A4 -60mV: n=12. A4G2 50mV: n=4. A4G2 -60mV: n=5.

During repeated stimulation, receptors became activated and desensitized at each stimulation. Depending on the decay rate of the desensitization, a certain percentage of receptors remained desensitized and would not be activated at the next stimulation, leading to a lower peak current at the next stimulation. Longer desensitization lead to less receptors being available at the next stimulation, so a larger drop in conductance at the beginning of the recording, and a lower normalized current once the system had reached an equilibrium. During 10 Hz stimulation, A4G2 condition recordings at both holding potentials showed weak but observable desensitization, apparent as a reduction in normalized peak current for each stimulation at the start of the recording, and a leveling out of these normalized peak currents over time (Fig. 5). Compared to both controls at 50 mV holding potentials, this was a stronger desensitization (Fig. 5 top). The variance between recordings for each of the control recordings at -60 mV was too large for an assessment of the shape of the curve and comparison with A2G4 (Fig 5. bottom).
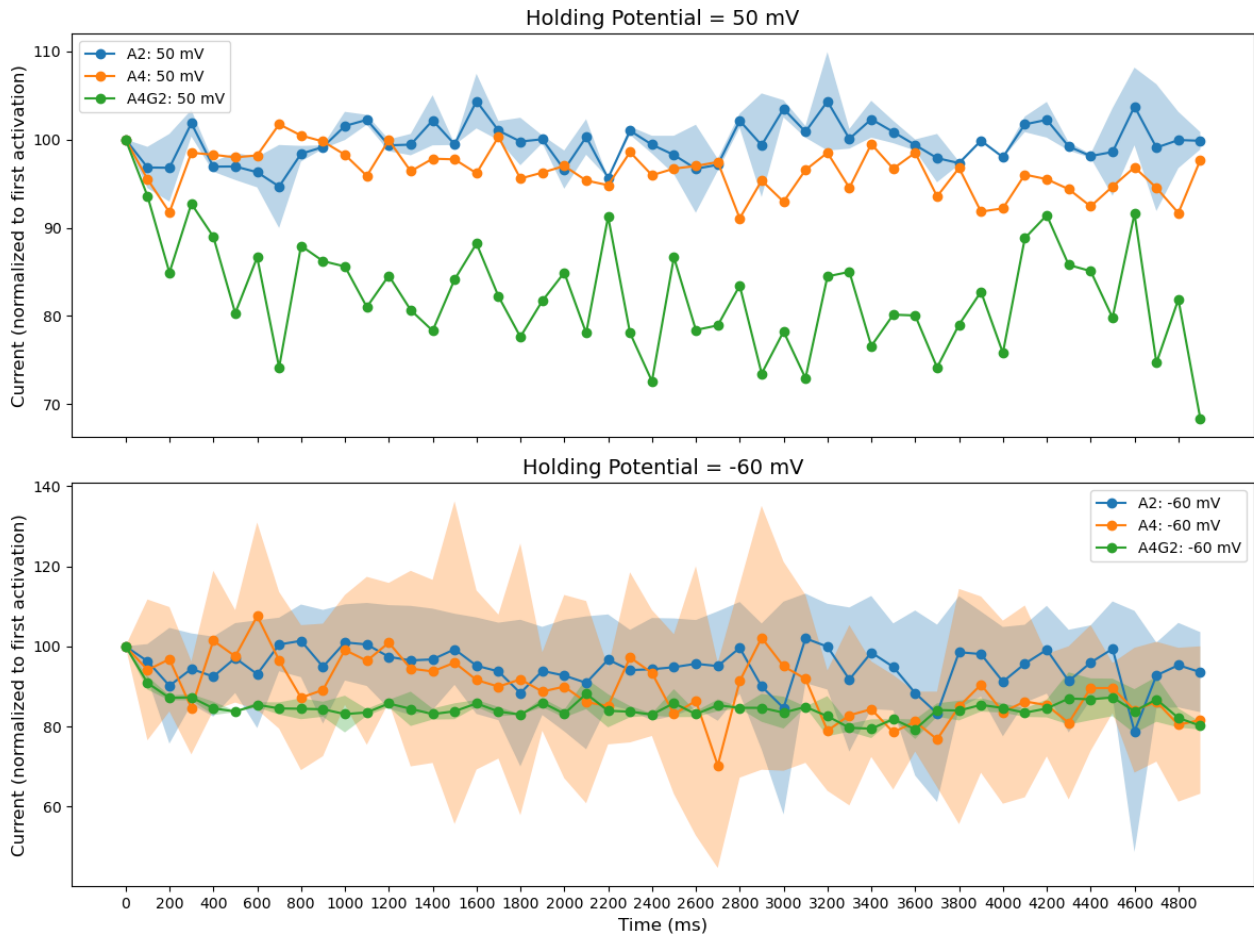
Figure 5. Desensitization during 10Hz stimulation. *Peak current of each 2 ms glutamate pulse, normalized to peak current of initial glutamate pulse, in %. A2 50mV: n=2. A4 50mV: n=1. A4G2 50mV: n=1. A2 -60mV: n=3. A4 -60mV: n=2. A4G2 -60mV: n=2.*

For 20Hz stimulation, no recordings of the A2 conditions were of high enough quality to analyze fully. The recordings showed desensitization across all conditions (Fig. 6) with more desensitization when compared to the 10 Hz protocol (Fig. 5). This was to be expected, as less time between each pulse meant more receptors were desensitized at the next pulse, leading to lower peak currents. Across both holding potentials, the A4 condition showed weaker desensitization than the A4G2 condition (Fig. 6). For 50Hz stimulation, no recordings in any condition were of high enough quality to be fully analyzed.

The decay of the current during glutamate exposure was driven by desensitization of the receptor. Significant differences between the weighted τ of the exponentials fitted to these traces were found between the A4G2 condition at -60 mV and the A4 condition -60 mV, determined by Mann-Whitney U test (p-value = 0.04148), the A2 condition at 50 mV and A4 condition at -60 mV, determined by Mann-Whitney U test (p-value = 0.00440), and the A2 condition at -60 mV and the A4 condition at -60 mV, determined by Mann-Whitney U test p-value = 0.02967 (Fig. 7 left). Notably, all comparisons include the A4 condition at -60 mV for which 12 separate recordings were analyzed. With such a high n compared to all other samples, finding significant differences here was unsurprising.
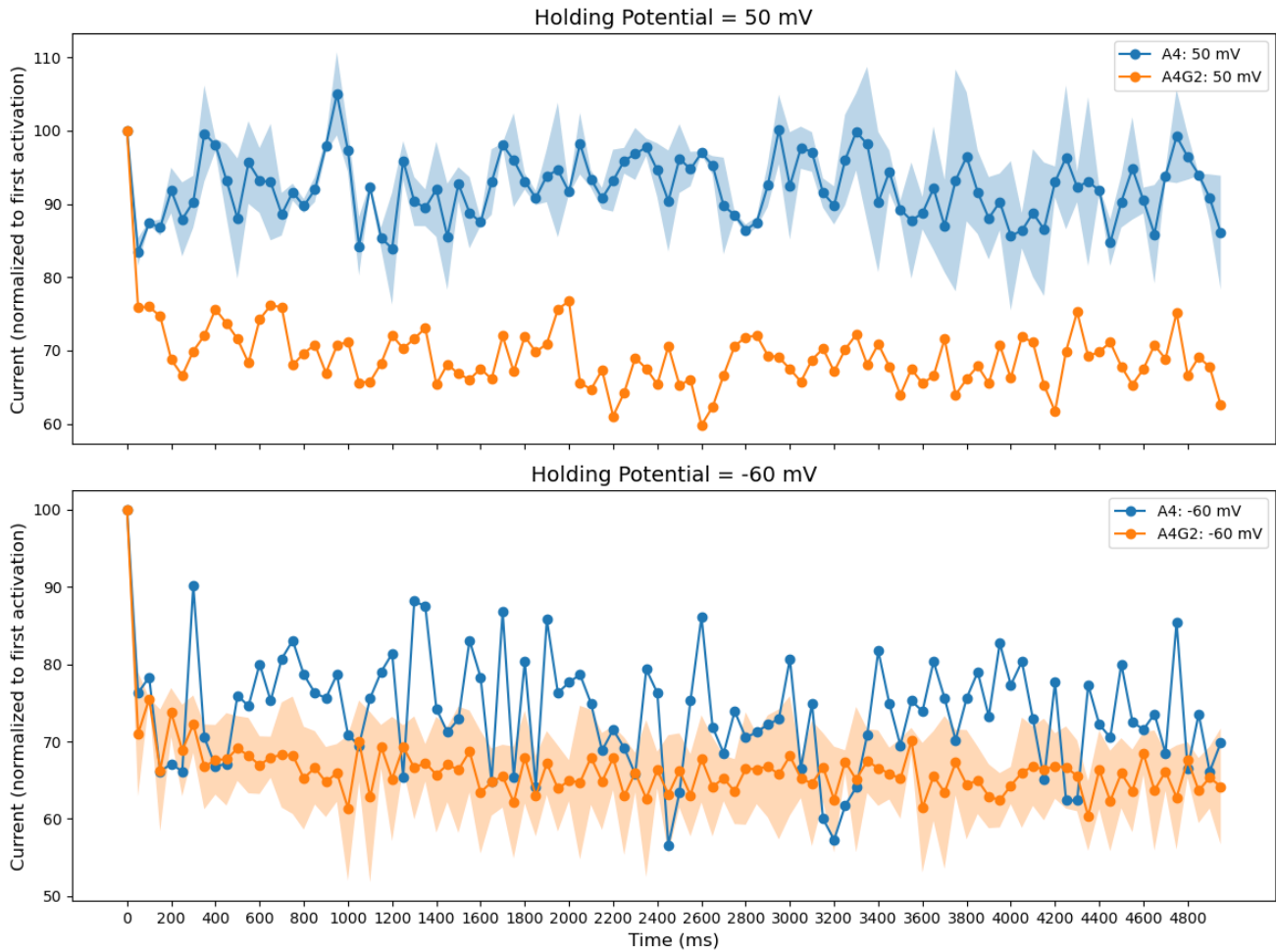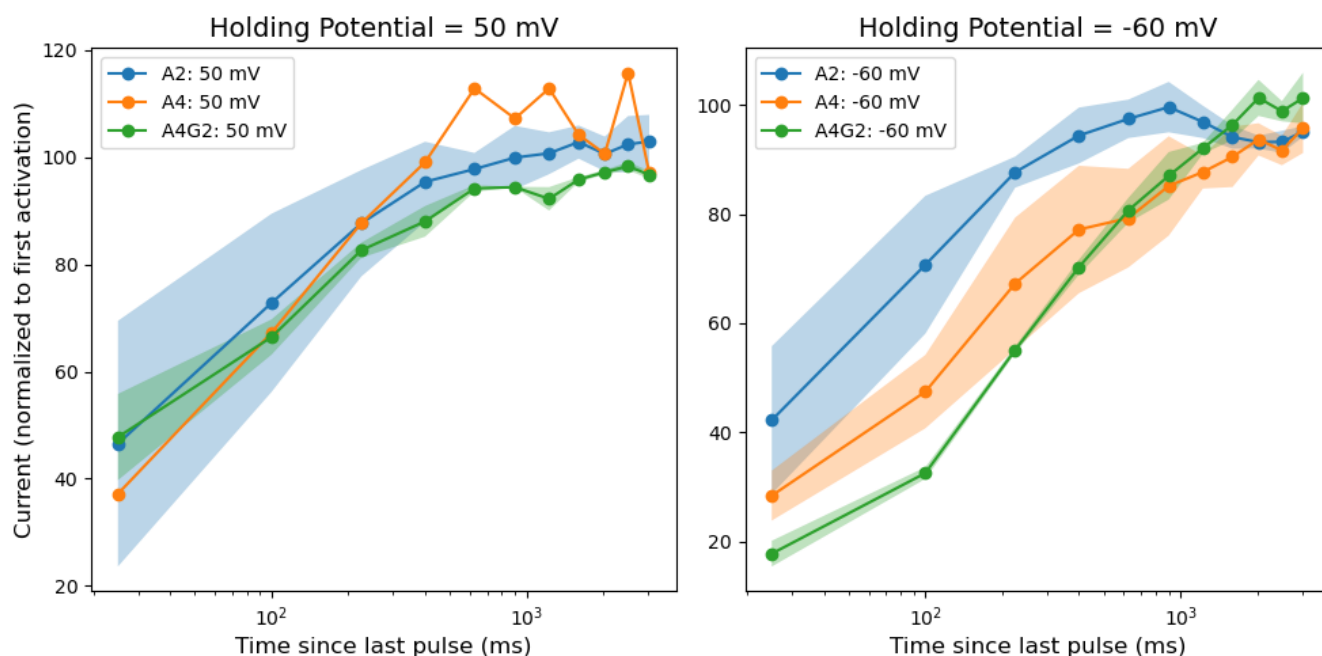
Figure 6. Desensitization during 20Hz stimulation. *Peak current of each 2 ms glutamate pulse, normalized to peak current of initial glutamate pulse, in %. A4 50mV: n=2. A4G2 50mV: n=1 A4 -60mV: n=1. A4G2 -60mV: n=2.*
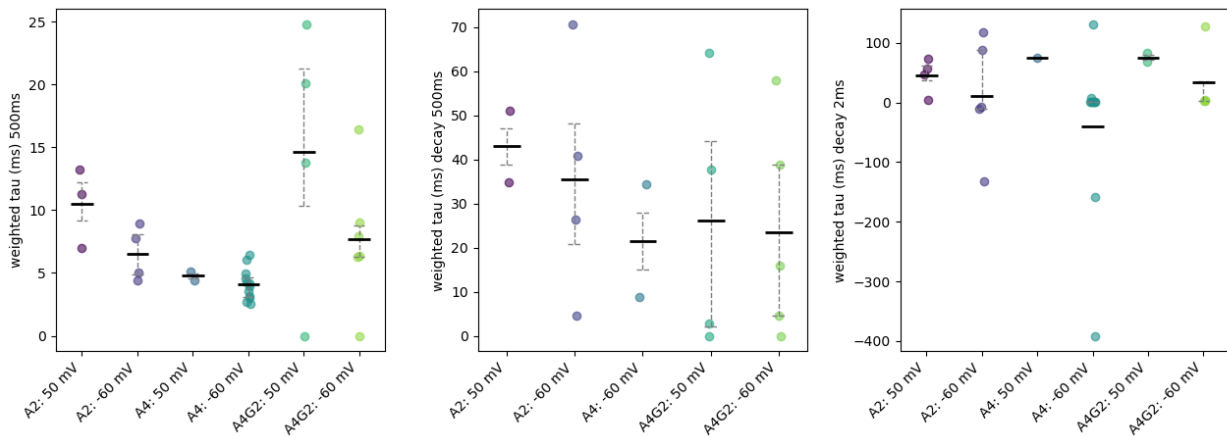
Figure 7. Kinetics. left: Desensitization. *Weighted τ (ms) of exponentials fitted to trace during 500 ms glutamate pulse. A2 50mV: n=3. A2 -60mV: n=4. A4 50mV: n=2. A4 -60mV: n=12. A4G2 50mV: n=4. A4G2 -60mV: n=5.* **middle: Decay.** *Weighted τ (ms) of exponentials fitted to trace after 500 ms glutamate pulse. A2 50mV: n=2. A2 -60mV: n=4. A4 -60mV: n=2. A4G2 50mV: n=2. A4G2 -60mV: n=4.* **right: Desensitization.** *Weighted τ (ms) of exponentials fitted to trace after 2 ms glutamate pulse. A2 50mV: n=4. A2 -60mV: n=5. A4 50mV: n=1. A4 -60mV: n=10. A4G2 50mV: n=3. A4G2 -60mV: n=3.*

The decay of the trace after the end of glutamate exposure corresponded to the lifetime of the open state after the end of glutamate exposure. This curve should be dominated by the unbinding constant of glutamate from the receptor, as open states without glutamate bound do not exist in any meaningful capacity. No significant differences were found in the weighted τ of these decay curves, determined by Kruskal-Wallis test (p-value = 0.80976). (Fig. 7 middle)

The decay after a 2 ms glutamate pulse more closely resembled an actual physiological activation of the receptors, as the glutamate concentration in the synaptic cleft rapidly decreases after synaptic release events. The component processes in this decay curve were therefore both desensitization, and unbinding of glutamate. No significant differences were found in the weighted τ of these curves, determined by Kruskal-Wallis test (p-value = 0.11585). (Fig. 7 right) Negative values for the weighted τ were caused by incorrect baseline correction for the traces of these recordings, leading to exponentials being fit to negative values.

Figure 8. Recovery from desensitization. *Incremental protocol: Peak current of each 25 ms glutamate pulse, excluding initial 500 ms pulse. Normalized to peak current of initial 500 glutamate pulse, in % plotted against log time since last pulse in ms. A2 50mV: n=3. A2 -60mV: n=3. A4 50mV: n=1. A4 -60mV: n=5. A4G2 50mV: n=3. A4G2 -60mV: n=3.*

The incremental protocol, with progressively more time in between glutamate pulses, allowed for an easy visualization of the recovery from desensitization, starting with completely desensitized receptors after a long initial glutamate pulse. When the exposure to glutamate was ended, some receptors recovered from desensitization and could open at the next glutamate pulse. The longer in between each pulse, the more receptors could recover, and the higher the current at the next event was. The speed of this recovery corresponded to the average lifetime of the desensitized state after the end of glutamate exposure. At 50 mV, there were no obvious differences between the recovery curves, mostly due to the A4 condition having n=1, and the A2 condition having large variance (Fig. 8 left). However, at -60 mV,

the A2 condition showed faster recovery than the A4 condition, and both A2 and A4 were faster than the A2G4 condition (Fig. 8 right), indicating that the γ-2 subunit lengthened the recovery from desensitization.
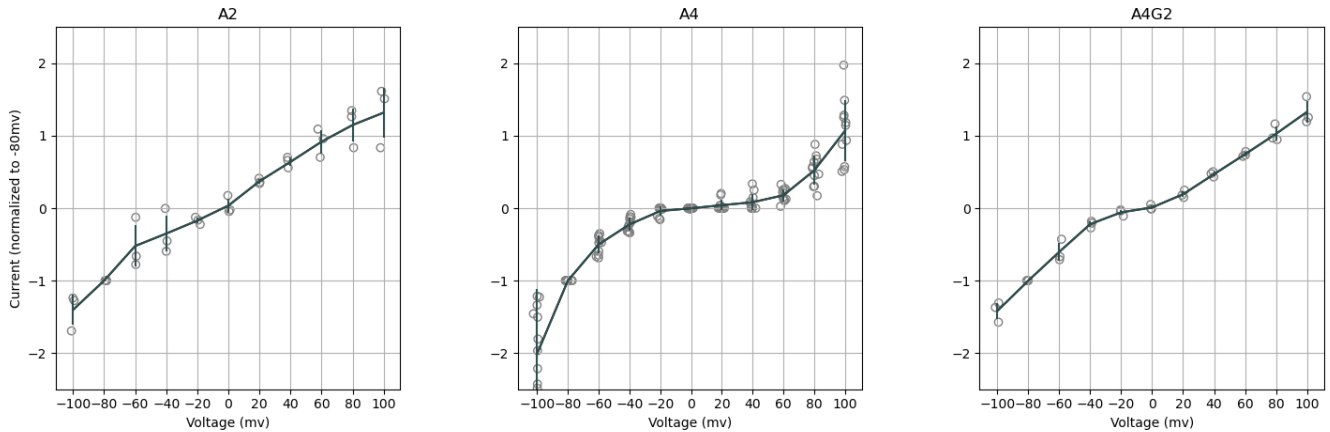
Figure 9. Voltage Dependency: I-V curves*. Peak current of glutamate pulse at each holding potential, normalized to peak current of glutamate pulse at -80 mV. A2: n=3. A4: n=11. A4G2: n=3.*

The voltage dependency of the receptor was determined by plotting the peak current upon stimulation by glutamate pulse for a range of holding potentials, resulting in an IV curve. The curve of the A2 condition was linear across the whole range of holding potentials (Fig. 9 left). Recordings for this condition had no spermine in the intracellular solution, so there was no polyamine block at low absolute holding potentials. The A2 condition was not a good control, since the A4 condition or the A4G2 condition did have spermine in the intracellular solution. It mostly served as an introduction to patching. The A4 condition showed a nonlinear IV curve, with very low peak currents close from about -20 mV to 40 mV (Fig. 9 middle). This was the range in which the polyamine block is strongest in ionotropic glutamate receptors, so this result was to be expected (Bowie 2018). The A4G2 condition, however, again showed a linear voltage dependency, indicating that the γ-2 subunit modulated the polyamine block. (Fig. 9 right)

3.2 Single channel analysis

Initially, for each episode, an idealized trace was reconstructed from the available events list .csv file. The activation time was also taken from the available .csv file, and to take into account the idealization, half the resolution time (65 μs) was added. When plotting all episodes from one recording of T1 in EDTA+CTZ in a scatter plot with marginal histograms (Fig. 10 left), it becomes apparent that, for most episodes, the amplitude of the idealized trace at the predefined activation time is 0. As the first event must, by definition, not have an amplitude of 0, this definition of a first event was unsatisfactory.

In a second attempt to define the first event, for each episode, again using the available predefined events list and activation table, the first event after first activation plus dead time

that had a drop in absolute amplitude was set as first event. These events were deemed "maximal first events" (Fig. 10 right) While this definition solved the problem of firsts event with a conductance of 0.0 being detected, as there was no way an event with a conductance of 0.0 could be followed by a drop in absolute conductance, it was also unsatisfactory. The time difference between the first activation and the start of the event defined as first event could be quite large, putting into question the purpose of the first activation detection itself. If the event containing the first activation time had an amplitude of 0.0 as well as no drop in absolute amplitude until the highest subconductance state, the event detected as the first events could be up to four events after the event where first actiation was detected. Additionally, there was no mechanistic significance to the first drop in conductance, there was no reason this event should hold any more information than the events the idealization algorithm detected before the maximal first events.
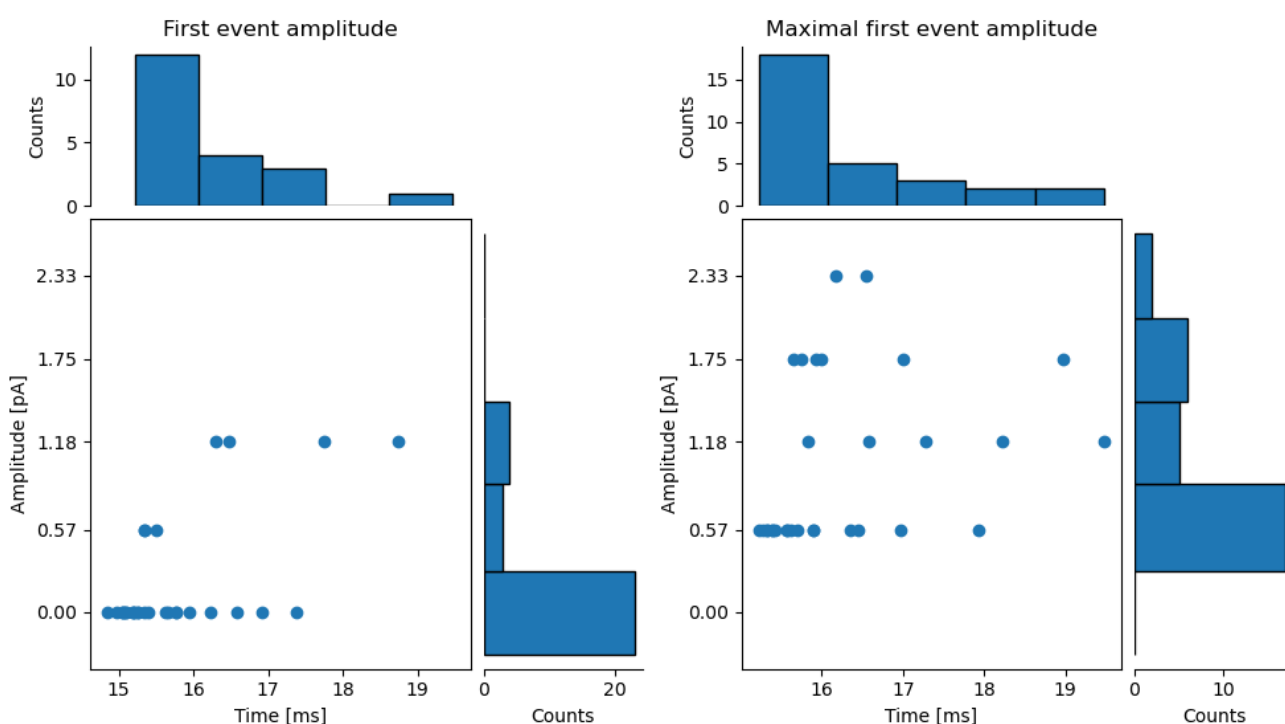

Figure 10. left: First event amplitude. *Absolute amplitude in pA of predefined idealized trace at predefined activation time in ms.* ***right: Maximal first event amplitude.*** *Absolute amplitude in pA and start time in ms of nonzero event before first drop in absolute amplitude in idealized trace after t0. Data from recording 19 on 25.10.2017 (T1 mutant in EDTA and CTZ)*

To be able to better develop the first events analysis, as well as to have this analysis available to others with similar research questions, further implementation was done directly in ASCAM. First, to solve a different problem that was encountered with many episodes, the parameter "exclusion time" was added to the first activation analysis page in ASCAM. For many episodes, the trace crossed the first activation threshold at the very start of the episode, presumably as an artefact of the filtering. This resulted in many episodes having a falsely detected first

activation, and the episode needing to be excluded or manually reviewed. By excluding the first couple of milliseconds from the threshold crossing algorithm, a lot more episodes could be used than previously, without manual review.

To detect the first event, the first activation was determined via threshold crossing as before. Then, dead time to account for the resolution of the idealization was added to determine the first event time point t. If the amplitude of the idealized trace at t was not 0, the event containing t was defined as first event. Otherwise, if the idealized trace at t was 0, the next event was defined as first event. A table of first event times, amplitudes and episode number could then be generated and exported. For the following data, only the previously idealized recordings were used. Threshold for first event detection was set at -0.5 pA and exclusion time at 10 ms. The subconductance state amplitudes were kept the same as for the previous idealizations. The first events detection was run on every recording that had previously idealized.
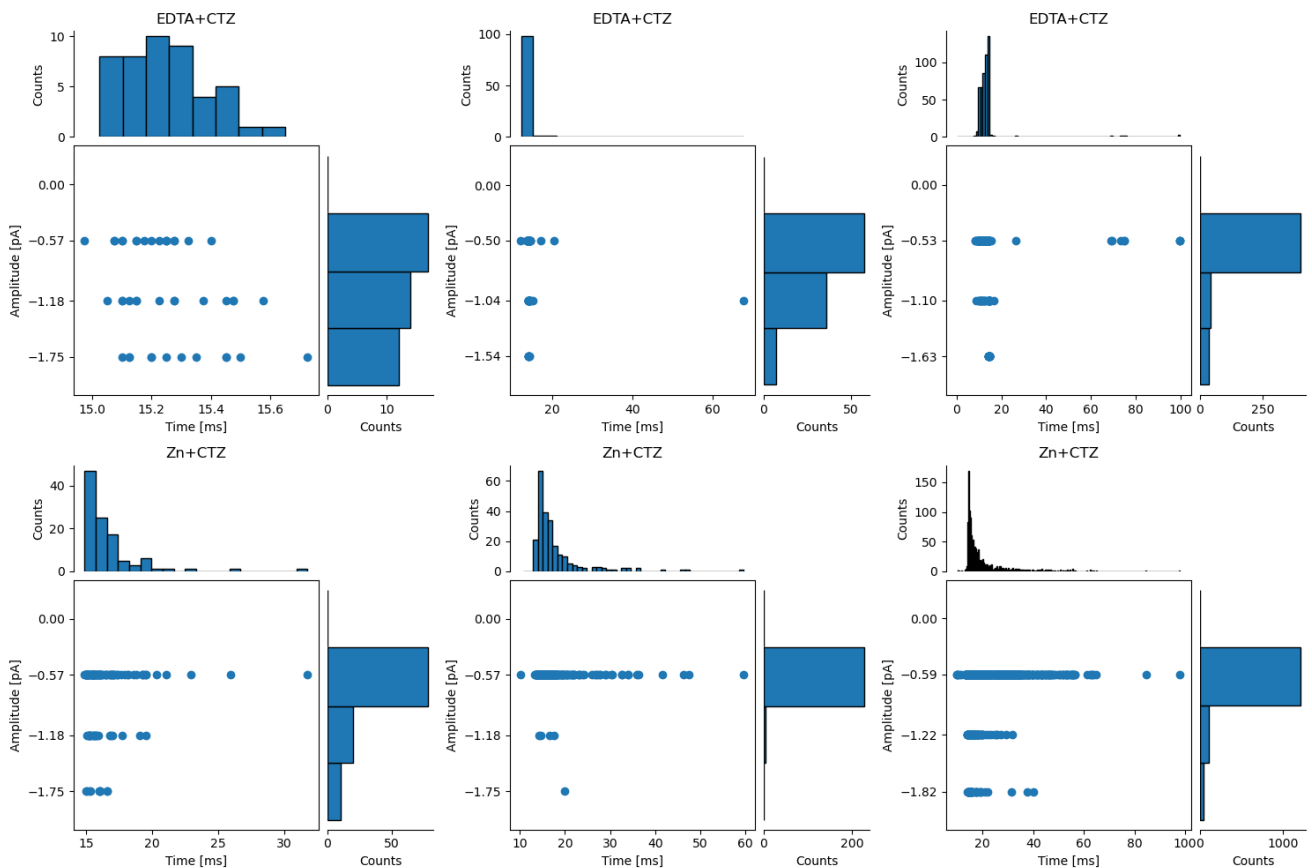

Figure 11. First event amplitude. *Amplitude in pA and start time in ms of first event. For T1 in EDTA and CTZ: Recording 19 from 25.10.2017 (left), recording 24 from 25.01.2018 (middle) and recording 4 from 18.05.2018 (right). For T1 in zinc and CTZ: Recording 24 from 24.01.2018 (left), recording 0 from 26.04.2018 (middle) and recording 14 07.05.2018 (right).*

Across all recordings, the most common first event amplitude was the lowest subconductance state, especially in the recordings with the most episodes (Fig. 11 top right, bottom right). In the Markov model of receptor activation, this was the open state with most conformations (7-10), as well as the one nearest to the closed state, so that it was visited first was expected.

Notably, for the T1 in EDTA+CTZ condition, the amplitude distributions were flatter, with more episodes with first events of a higher subconductance state. This condition was expected to have faster activation kinetics than the zinc+CTZ condition, so intermediate states with a dwell time too short for the idealization to detect should have been more common, leading to bigger jumps in the idealized trace. This resulted in more first events with a high amplitude, leading to a flatter distribution of first event amplitudes.

Transitioning from closed to open state was a process that could be assumed to have equal probability across all time points, resulting in an exponential distribution of first latencies (Fig 11). In addition, first events opening to a higher subconductance states tended to be much earlier (Fig. 11). If the openings to different subconductance states had similar exponential distributions, one would expect to find a lot more early openings with a smaller sample size, which higher amplitude first events tend to have. Indeed, in the recording with the most similar number of openings for each subconductance state (Fig. 11 top left), the distributions of the activation times were more similar between first event amplitudes than in other recordings.

3.5 First latency histograms for each initial subconductance state
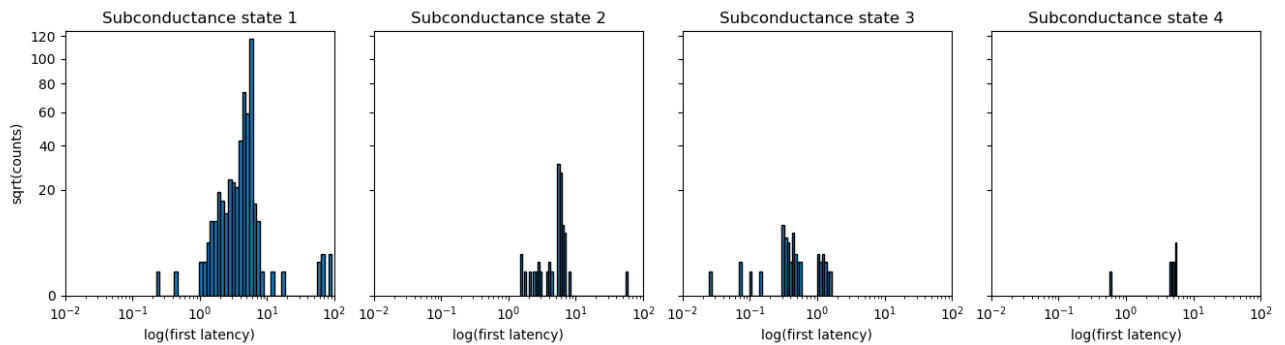
Figure 12. T1 mutant in EDTA and CTZ. First latency histogram for each initial subconductance state, with log(ms), square root(counts) scale. State 1: ~-0.55 pA. State 2: ~-1.10 pA. State 3: ~-1.61 pA. State 4: ~-2.21 pA. Data pooled from 3 recordings.
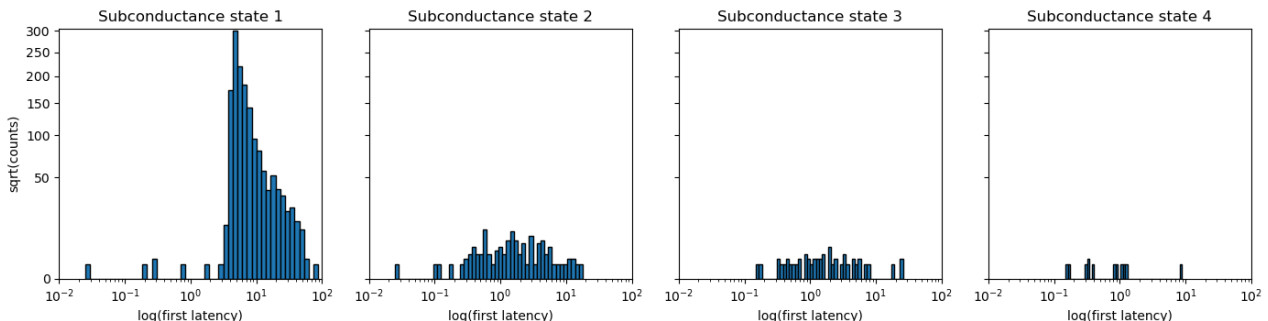
Figure 13. T1 mutant in zinc and CTZ. First latency histogram for each initial subconductance state, with log(ms), square root(counts) scale. State 1: ~-58 pA. State 2: ~-1.20 pA. State 3: ~-1.77 pA. State 4: ~-2.37 pA. Data pooled from 3 recordings.

When examining the first latency distributions separately for each subconductance state and plotting them on a log square root scaled histogram, what became most readily apparent was

the much slower activation times of the zinc+CTZ condition. All the distributions were further right on the logarithmic time scale in the zinc+CTZ condition compared to the EDTA+CTZ condition (Fig. 12, Fig. 13). In the histograms for subconductance state 1, there seemed to be some humps in the distributions for both conditions, indicating there might be a multimodal distribution with more than one component. However, without fitting exponentials to these distributions, no quantitative assessment of the number or time constants of the components in these distributions could be made. For higher subconductance state first events, there was not enough data for any robust conclusions to be drawn from the distribution, for either condition (Fig. 12 middle and right, Fig. 13 middle and right).

4 Discussion

4.1 Characterization of the GluA4 γ-2 tandem

There were no significant differences between any of the kinetic parameters, with one exception. This is probably due to the low number of recordings available for each condition and holding potential. The one condition that showed significant differences with other conditions, A4 at -60mV, had an *n* of 12, compared to the *n* of 1-5 of other conditions. More recordings from all conditions are necessary to achieve the statistical power necessary for robust differentiation of the electrophysiological properties of these receptor constructs.

The quality of the recordings also might skew the results. Most of the GluA4 recordings used for analysis had a comparatively small peak current, in large part due to the quality of the patch. TARPs usually aid in receptor trafficking to the membrane as well, which could also explain the comparatively higher peak current of the A4G2 condition (Milstein & Nicoll, 2009). The lower peak current led to a high contribution of change in osmolarity due to solution exchange to the total current during stimulation. The resulting higher steady state current influenced the shape of the trace that the exponentials were fit to, and thus the kinetic parameters. In addition, the systematically higher current during stimulation might have led to underestimation of desensitization.

Previously, when co-expressing GluA2 or GluA4 with γ-2 in Hek293 cells and recording using incremental and pulse train protocols, a distinct type of electrophysiological response deemed superactivation was observed. Superactivation was characterized by an increase in peak current during repeated stimulation and continued stimulation, respectively, after desensitization. This was proposed to be caused by distinct high conductance superactivated state, which could only be achieved in the presence of TARPs, which could only be reached after desensitization and had far slower activation kinetics than the normal open state. In addition, the presence of even small amounts of TARPs caused weaker desensitization,

presumably because of a certain small percentage of superactivated receptors (Carbone & Plested, 2016).

These findings do not match with my observations. The A4G2 condition showed stronger desensitization compared to both controls in the repeated stimulation protocols, across all conditions, in so far as this was ascertainable (Fig. 5, Fig. 6). For recovery from desensitization, at -60 mV, the A4G2 condition showed slower recovery from desensitization than both controls, and no superactivation (Fig. 8). There was also no significant difference between the normalized steady state percentage between all conditions and holding potentials, though this was probably due to low recording numbers or quality.

This difference could be caused by the different construct used. The tandem contains a linker, to ensure that every GluA4 subunit has exactly one γ-2. The stoichiometry of the different proteins, or the linker itself could somehow interfere with the stability of the superactivated state. CryoEM structures of GluA4 or GluA2 in the presence of γ-2 or γ8, compared to those connected via linker, as well as glutamate and CTZ could shed light on the exact stoichiometry or confirmation needed to achieve the superactivated state. Electrophysiologically characterizing other, even heteromeric combinations of GluA subunits with TARPs could also prove useful in this regard. Alternatively, this mismatch in findings could be caused by the low number and low quality of the recordings available for analysis. Determining the charge, transfer during pulse train stimulation, could also help characterize this construct further and compare it with previous findings.

4.2 single channel analysis

The two first definitions of the first events analysis were unsatisfactory. However, there was valuable insight to be gained about the idealization itself, and how the first events should be defined. The events in the previous idealization did not correlate with the first activations at all. For a range of dead times, there were still first events with an amplitude of 0.0, when defining first event as the amplitude in the idealized trace at the first activation time point. This showed that simply taking the first activation as the time point for first event detection was insufficient, and the first event detection needed to take into consideration events before the detected first activation. Defining the first event before a drop in absolute current as first event was also unsatisfactory, as there was no mechanistic significance to this specific event. However, the idea of focusing on more complicated events that consist of more than one conductance state, could be promising. For example, it could help improve determine rate constants. Histograms of dwell times in these more complex states, to compare the estimation of the rate constants of the Markov model in the simulation to real data, could lead to a more accurate model fit.

As with all single channel patch clamp experiments, the noise of the setup is a limiting factor for the quality of the analysis that is based on the recordings. Additionally, the sample size of high-quality recordings to choose from is limited, without going through the whole work of setting up the whole experiment again. However, even for the conditions that were analysed for this work, T1 in CTZ+EDTA and CTZ+zinc, some high-quality recordings that have not been analysed still exist. Additionally, the recordings that exist for WT in CTZ+EDTA and CTZ+zinc should be analysed the same way to serve as control. Concatenating all first events for each condition should ideally yield distributions with sufficient data points for fitting exponentials, ideally for every condition. Exponentials should then be fit to these distributions, to find the number and time constants of the components, and to allow for conclusions about the underlying states.

Most important for this analysis, however, was the effect of the idealization, as it directly determines the start and stopping times for each event, as well as the amplitude. In the idealization, the most important parameter for this analysis was resolution. Too long of a resolution led to short events being missed, while to small of a resolution led to overfitting of noise. The parameters for the idealization algorithm and filtering steps in these recordings should be optimized, to reach the most robust idealization, and thus the most robust first event detection. In addition, the effect of the resolution of the idealization on the final data should be studied in future work.

In ASCAM, finding a way to automatically save the resolution of the idealization and to apply half of it as the dead time in the first event detection would be helpful. An error widget for handling the error of running the first event detection before an idealization has been run or imported, would greatly increase the user experience. Benchmarking the automatic first event detection against manual detection would help assess the algorithms applicability. In addition, quantitatively assessing the effects of the idealization resolution on the result of the first event detection would help finding optimal parameters for both algorithms.

References

Anggono, V., & Huganir, R. L. (2012). Regulation of AMPA Receptor Trafficking and Synaptic

Plasticity. *Current Opinion in Neurobiology*, *22*(3), 461–469.

https://doi.org/10.1016/j.conb.2011.12.006

Armstrong, N., & Gouaux, E. (2000). Mechanisms for activation and antagonism of an AMPA-

sensitive glutamate receptor: Crystal structures of the GluR2 ligand binding core. *Neuron*,

28(1), 165–181. https://doi.org/10.1016/s0896-6273(00)00094-5

Baranovic, J., Chebli, M., Salazar, H., Carbone, A. L., Faelber, K., Lau, A. Y., Daumke, O., & Plested, A. J. R. (2016). Dynamics of the Ligand Binding Domain Layer during AMPA Receptor Activation. *Biophysical Journal*, *110*(4), 896–911. https://doi.org/10.1016/j.bpj.2015.12.033

Blanke, M. L., & VanDongen, A. M. J. (2009). Activation Mechanisms of the NMDA Receptor. In A. M. Van Dongen (Ed.), *Biology of the NMDA Receptor*. CRC Press/Taylor & Francis. http://www.ncbi.nlm.nih.gov/books/NBK5274/

Bowie, D. (2018). Polyamine-mediated channel block of ionotropic glutamate receptors and its regulation by auxiliary proteins. *Journal of Biological Chemistry*, *293*(48), 18789–18802. https://doi.org/10.1074/jbc.TM118.003794

Braunbeck, S. (2022). *Analysis of the activation of AMPA-type glutamate receptors at the single-channel level*. Humboldt-Universität zu Berlin. https://doi.org/10.18452/23955

Carbone, A. L., & Plested, A. J. R. (2016). Superactivation of AMPA receptors by auxiliary proteins. *Nature Communications*, *7*(1), 10178. https://doi.org/10.1038/ncomms10178

Chen, S., Zhao, Y., Wang, Y., Shekhar, M., Tajkhorshid, E., & Gouaux, E. (2017). Activation and Desensitization Mechanism of AMPA Receptor-TARP Complex by Cryo-EM. *Cell*, *170*(6), 1234-1246.e14. https://doi.org/10.1016/j.cell.2017.07.045

Collingridge, G. L., & Lester, R. A. (1989). Excitatory amino acid receptors in the vertebrate central nervous system. *Pharmacological Reviews*, *41*(2), 143–210.

Colquhoun, D., Jonas, P., & Sakmann, B. (1992). Action of brief pulses of glutamate on AMPA/kainate receptors in patches from different neurones of rat hippocampal slices. *The Journal of Physiology*, *458*, 261–287. https://doi.org/10.1113/jphysiol.1992.sp019417

Derkach, V. A., Oh, M. C., Guire, E. S., & Soderling, T. R. (2007). Regulatory mechanisms of AMPA receptors in synaptic plasticity. *Nature Reviews Neuroscience*, *8*(2), 101–113. https://doi.org/10.1038/nrn2055

Dingledine, R., Borges, K., Bowie, D., & Traynelis, S. F. (1999). The glutamate receptor ion channels. *Pharmacological Reviews*, *51*(1), 7–61.

Esmenjaud, J., Stroebel, D., Chan, K., Grand, T., David, M., Wollmuth, L. P., Taly, A., & Paoletti, P. (2019). An inter-dimer allosteric switch controls NMDA receptor activity. *The EMBO Journal*, *38*(2), e99894. https://doi.org/10.15252/embj.201899894

Fucile, S., Miledi, R., & Eusebi, F. (2006). Effects of cyclothiazide on GluR1/AMPA receptors. *Proceedings of the National Academy of Sciences of the United States of America*, *103*(8), 2943–2947. https://doi.org/10.1073/pnas.0511063103

Geiger, J. R., Melcher, T., Koh, D. S., Sakmann, B., Seeburg, P. H., Jonas, P., & Monyer, H. (1995). Relative abundance of subunit mRNAs determines gating and Ca2+ permeability of AMPA receptors in principal neurons and interneurons in rat CNS. *Neuron*, *15*(1), 193–204. https://doi.org/10.1016/0896-6273(95)90076-4

Greger, I. H., Watson, J. F., & Cull-Candy, S. G. (2017). Structural and Functional Architecture of AMPA-Type Glutamate Receptors and Their Auxiliary Proteins. *Neuron*, *94*(4), 713–730. https://doi.org/10.1016/j.neuron.2017.04.009

Herguedas, B., Krieger, J., & Greger, I. H. (2013). Receptor heteromeric assembly-how it works and why it matters: The case of ionotropic glutamate receptors. *Progress in Molecular Biology and Translational Science*, *117*, 361–386. https://doi.org/10.1016/B978-0-12-386931-9.00013-1

Huganir, R. L., & Nicoll, R. A. (2013). AMPARs and Synaptic Plasticity: The Last 25 Years. *Neuron*, *80*(3), 704–717. https://doi.org/10.1016/j.neuron.2013.10.025

Hunter, J. D. (2007). Matplotlib: A 2D graphics environment. Computing in Science & Engineering, 9(3), 90–95. (n.d.). [Computer software].

Italia, M., Ferrari, E., Di Luca, M., & Gardoni, F. (2021). GluA3-containing AMPA receptors: From physiology to synaptic dysfunction in brain disorders. *Neurobiology of Disease*, *161*, 105539. https://doi.org/10.1016/j.nbd.2021.105539

Krugers, H. J., Hoogenraad, C. C., & Groc, L. (2010). Stress hormones and AMPA receptor trafficking in synaptic plasticity and memory. *Nature Reviews Neuroscience*, *11*(10), 675–681. https://doi.org/10.1038/nrn2913

Kuner, T., Seeburg, P. H., & Guy, H. R. (2003). A common architecture for K+ channels and ionotropic glutamate receptors? *Trends in Neurosciences*, *26*(1), 27–32. https://doi.org/10.1016/s0166-2236(02)00010-3

Kuru, E. (2024). *Comparison of Idealization Algorithms to Analyze Single Channel Recordings and Their Application to AMPA Receptor Sublevel Kinetics*.

Lewis, D. A., & Moghaddam, B. (2006). Cognitive Dysfunction in Schizophrenia: Convergence of γ-Aminobutyric Acid and Glutamate Alterations. *Archives of Neurology*, *63*(10), 1372–1376. https://doi.org/10.1001/archneur.63.10.1372

Meldrum, B. S. (2000). Glutamate as a Neurotransmitter in the Brain: Review of Physiology and Pathology. *The Journal of Nutrition*, *130*(4), 1007S-1015S. https://doi.org/10.1093/jn/130.4.1007S

Milstein, A. D., & Nicoll, R. A. (2009). TARP modulation of synaptic AMPA receptor trafficking and gating depends on multiple intracellular domains. *Proceedings of the National Academy of Sciences*, *106*(27), 11348–11351. https://doi.org/10.1073/pnas.0905570106

Pampaloni, N. P., Riva, I., Carbone, A. L., & Plested, A. J. R. (2021). Slow AMPA receptors in hippocampal principal cells. *Cell Reports*, *36*(5), 109496. https://doi.org/10.1016/j.celrep.2021.109496

Partin, K. M., Bowie, D., & Mayer, M. L. (1995). Structural determinants of allosteric regulation in alternatively spliced AMPA receptors. *Neuron*, *14*(4), 833–843. https://doi.org/10.1016/0896-6273(95)90227-9

Pereyra, M., & Medina, J. H. (2021). AMPA Receptors: A Key Piece in the Puzzle of Memory Retrieval. *Frontiers in Human Neuroscience*, *15*, 729051. https://doi.org/10.3389/fnhum.2021.729051

Picconi, B., Piccoli, G., & Calabresi, P. (2012). Synaptic Dysfunction in Parkinson's Disease. In M. R. Kreutz & C. Sala (Eds.), *Synaptic Plasticity: Dynamics, Development and Disease* (pp. 553–572). Springer. https://doi.org/10.1007/978-3-7091-0932-8_24

Plested, A. J. R., & Mayer, M. L. (2009). AMPA Receptor Ligand Binding Domain Mobility Revealed by Functional Cross Linking. *The Journal of Neuroscience*, *29*(38), 11912–11923. https://doi.org/10.1523/JNEUROSCI.2971-09.2009

Rosenmund, C., Stern-Bach, Y., & Stevens, C. F. (1998). The tetrameric structure of a glutamate receptor channel. *Science (New York, N.Y.)*, *280*(5369), 1596–1599. https://doi.org/10.1126/science.280.5369.1596

Sanderson, D. J., Good, M. A., Seeburg, P. H., Sprengel, R., Rawlins, J. N. P., & Bannerman, D. M. (2008). Chapter 9 The role of the GluR-A (GluR1) AMPA receptor subunit in learning and

memory. In W. S. Sossin, J.-C. Lacaille, V. F. Castellucci, & S. Belleville (Eds.), *Progress in Brain Research* (Vol. 169, pp. 159–178). Elsevier. https://doi.org/10.1016/S0079-6123(07)00009-X

Silver, R. A., Traynelis, S. F., & Cull-Candy, S. G. (1992). Rapid-time-course miniature and evoked excitatory currents at cerebellar synapses in situ. *Nature*, *355*(6356), 163–166. https://doi.org/10.1038/355163a0

Sobolevsky, A. I., Rosconi, M. P., & Gouaux, E. (2009). X-ray structure, symmetry and mechanism of an AMPA-subtype glutamate receptor. *Nature*, *462*(7274), 745–756. https://doi.org/10.1038/nature08624

Stern-Bach, Y., Russo, S., Neuman, M., & Rosenmund, C. (1998). A Point Mutation in the Glutamate Binding Site Blocks Desensitization of AMPA Receptors. *Neuron*, *21*(4), 907–918. https://doi.org/10.1016/S0896-6273(00)80605-4

Swanson, G. T., Kamboj, S. K., & Cull-Candy, S. G. (1997). Single-channel properties of recombinant AMPA receptors depend on RNA editing, splice variation, and subunit composition. *The Journal of Neuroscience: The Official Journal of the Society for Neuroscience*, *17*(1), 58–69. https://doi.org/10.1523/JNEUROSCI.17-01-00058.1997

Traynelis, S. F., Wollmuth, L. P., McBain, C. J., Menniti, F. S., Vance, K. M., Ogden, K. K., Hansen, K. B., Yuan, H., Myers, S. J., & Dingledine, R. (2010). Glutamate receptor ion channels: Structure, regulation, and function. *Pharmacological Reviews*, *62*(3), 405–496. https://doi.org/10.1124/pr.109.002451

Van Rossum, G., & Drake, F. L. (2009). Python 3 Reference Manual. Scotts Valley, CA: CreateSpace. (n.d.). [Computer software].

Zarate, C. A., & Manji, H. K. (2008). The Role of AMPA Receptor Modulation in the Treatment of Neuropsychiatric Diseases. *Experimental Neurology*, *211*(1), 7–10. https://doi.org/10.1016/j.expneurol.2008.01.011

Zeppillo, T., Schulmann, A., Macciardi, F., Hjelm, B. E., Föcking, M., Sequeira, P. A., Guella, I., Cotter, D., Bunney, W. E., Limon, A., & Vawter, M. P. (2022). Functional impairment of cortical AMPA receptors in schizophrenia. *Schizophrenia Research*, *249*, 25–37. https://doi.org/10.1016/j.schres.2020.03.037

Lukas Born

Zhang, W., Devi, S. P. S., Tomita, S., & Howe, J. R. (2014). Auxiliary proteins promote modal gating

of AMPA- and kainate-type glutamate receptors. *The European Journal of Neuroscience*,

39(7), 1138–1147. https://doi.org/10.1111/ejn.12519